



# Preparation and properties of porous ceramics from spodumene flotation tailings by low-temperature sintering

Jie YANG<sup>1</sup>, Long-hua XU<sup>1,2</sup>, Hou-qin WU<sup>1,3</sup>, Jiao JIN<sup>4</sup>

1. Key Laboratory of Solid Waste Treatment and Resource Recycle (Ministry of Education), Southwest University of Science and Technology, Mianyang 621010, China;
2. State Key Laboratory for Environment-friendly Energy Materials, Southwest University of Science and Technology, Mianyang 621010, China;
3. School of Civil Engineering and Architecture, Southwest University of Science and Technology, Mianyang 621010, China;
4. School of Traffic and Transportation Engineering, Changsha University of Science and Technology, Changsha 410114, China

Received 9 September 2020; accepted 8 April 2021

**Abstract:** Porous ceramics were prepared with spodumene flotation tailings (SFT), kaolin and low-melting point glass (LPG) powder, whose pores were formed by the chemical reaction of hydrogen peroxide ( $H_2O_2$ ). LPG was used to reduce the sintering temperature of porous ceramics and kaolin was used to realize the adsorption to methylene blue (MB) of porous ceramics. The average flexural strength, compressive strength, apparent porosity, water absorption and maximum MB adsorption capacity were 5.60 MPa, 4.66 MPa, 52.27%, 44.32% and 0.7 mg/g, respectively. Moreover, the results of orthogonal experiments present that the sintering temperature and the dosage of  $H_2O_2$  had great influence on the mechanical properties and apparent porosity of porous ceramics, respectively. The main reason for the improvement of mechanical properties of porous ceramics was that LPG gradually became soft with increasing the sintering temperature, which made the mineral particles adhere to each other closely. Kaolinite was not completely converted into metakaolin at 550 °C, which might be the main reason why porous ceramics had adsorption properties.

**Key words:** spodumene flotation tailings; porous ceramics; low-temperature sintering; absorption

## 1 Introduction

In view of the outstanding physical and chemical properties, lithium with the least density is widely used in aeronautics, optical fields and energy storage especially in the lithium battery field [1–3]. Spodumene is one of the main sources of lithium and flotation is a dominant method to efficiently separate spodumene from gangue minerals [4–7]. Over the past few decades, as demands for mineral metals have increased, the volume of flotation tailings has increased

dramatically. Flotation tailings are common causes of environmental pollution. The risk of the accumulation of tailings is increasing due to the increasing amount of low grade ore and the effects of extreme weather [8,9]. Therefore, the great management and high reuse of flotation tailings contribute not only to the protection of the environment but also to the development of the world's economies. Therefore, proper storage and comprehensive utilization of flotation tailings have become focusing issues globally [10]. To date, solidification filling is still the main method to deal with the tremendous scale of tailings. In recent

years, plenty of research efforts have been put on the utilization of aluminosilicate containing waste in the manufacturing of porous ceramics [11,12]. Albite, quartz and microcline are main compositions of spodumene floatation tailings (SFT), which are consistent with the green materials of ceramic materials [13]. In the development process of comprehensive utilization of tailings, LEMOUGNA et al [14–16] have done a lot of useful studies including the preparation of building materials and ceramic materials, etc. However, There is still a long way to go in the development of novel, efficient and green utilization pathways [17].

On the other hand, with acute water scarcity and pollution, there is a crucial need to achieve a more sustainable management of the world's water resources. Efficient, convenient, energy-saving and sustainable water treatment methods face immense environmental and engineering challenges. Organic dyes are widely used in the industry fields of pharmaceuticals, food, paper, pulp manufacturing, plastic, cloth and printing. During dying process, a large amount of dyes have been mixed with effluent in inland water bodies [18,19]. Therefore, the removal of these pollutions from wastewater has become a critical issue around the world [20]. Some of these organics, which can inhibit the penetration of sunlight and oxygen are highly toxic to the environment, thus in-turn influencing the content of oxygen in the water which is essential for aquatic life [21]. Wastewater containing a high level of artificially synthesized organic pollutants poses a serious threat to water environment and human health [22]. Without a doubt, there is a crucial need to achieve a more sustainable management of the world's water resources with acute water scarcity and water pollution. Therefore, the development of efficient water management and treatment technologies is able to offer more feasible options to enhance the efficiency and quality of water treatment [23,24]. However, some organics cannot be completely removed by means of conventional biological treatment processes, such as an activated sludge and an anaerobic digestion: due to their low

biodegradability, nearly 90% of reactive dyes remain unchanged after undergoing an activated sludge process [25]. Therefore, adsorption materials have been widely investigated to treat organic wastewater [26].

Types and properties of adsorption materials are parts of the key factors affecting the adsorption effect. Commonly used adsorbents include activated carbon [27,28], chitosan [29,30] and kaolin [31,32]. Organic materials like activated carbon and chitosan can be decomposed through combustion at a high temperature. So, kaolin was selected as the adsorbent in this work. In order to reduce the sintering temperature of ceramic materials, low-melting point glass (LPG) was used as the binding material in this paper. Kaolin was employed as the loading adsorption material to generate adsorption properties of porous ceramics. The sintering mechanism was explored through the test of XRD, FT-IR, SEM-EDS and TGA-DSC.

## 2 Experimental

### 2.1 Raw materials

SFT used in this study was obtained from a concentrator in Ganzi Prefecture, Sichuan Province, China. Commercial kaolin and LPG powders were purchased for the study. The chemical composition of raw materials is given in Table 1. Sodium cardiomyopathy cellulose (CMC-Na) was chosen as a toughening agent for green bodies, with formula of  $[C_6H_7O_2(OH)_2OCH_2COONa]_n$ . The concentration of  $H_2O_2$  solution was 30%. The median particle sizes ( $d_{50}$ ) of SFT, kaolin, LPG were 61.62, 16.47 and 14.23  $\mu m$ , respectively.

### 2.2 Experimental procedure

The manufacturing processes of porous ceramics are presented in Fig. 1. The raw materials were put into an NJ-160 cement paste mixer with water (Wuxi Construction Engineering Test Equipment Co., Ltd.) and mixed for 4 min. Then,  $H_2O_2$  was added and stirring was continued for 1 min. Ceramics were shaped in rectangular prism

**Table 1** Chemical compositions of main raw materials (wt.%)

Raw material	SiO <sub>2</sub>	Al <sub>2</sub> O <sub>3</sub>	K <sub>2</sub> O	Na <sub>2</sub> O	CaO	Fe <sub>2</sub> O <sub>3</sub>	P <sub>2</sub> O <sub>5</sub>	Others
SFT	79.75	12.04	5.39	0.96	0.25	0.81	0.23	0.57
Kaolin	54.30	42.43	0.13	0.00	0.42	0.67	0.30	1.75
LPG	2.79	24.77	14.86	17.81	0.05	0	35.5	4.22

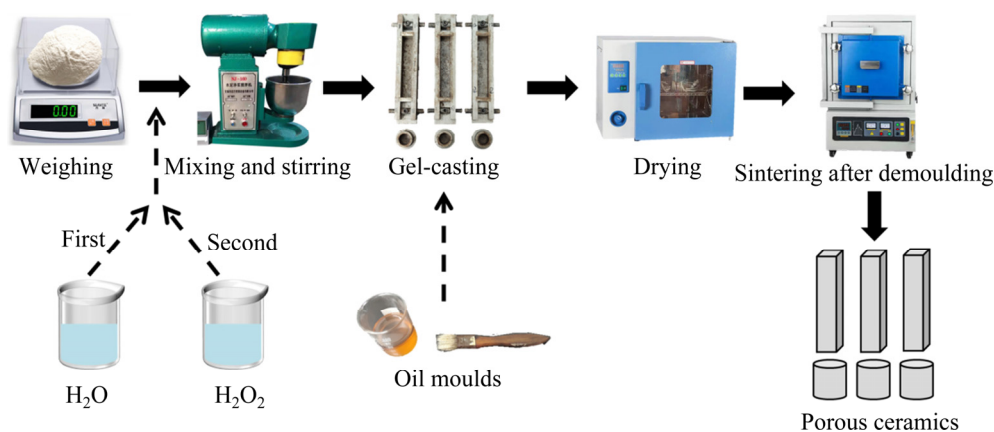


Fig. 1 Manufacturing process of porous ceramics

alloy moulds (120 mm × 20 mm × 20 mm) and cylindrical moulds ( $d20$  mm × 20 mm). After demoulding, they were dried at 120 °C for 24 h and a saw was used to cut off the surplus parts that overflow the mould in the foaming process. The samples were sintered in a medium-temperature XZWL-14-12Y test furnace (Sinosteel Luoyang Institute of Refractories Research Co., Ltd.). The heating rate was 8 °C/min and the holding time was 2 h at the maximum temperature. After the sintering process, samples were cooled down at 8 °C/min to 50 °C.

## 2.3 Physical properties

### 2.3.1 Flexural strength and compressive strength

The flexural strength was performed using a mechanical testing machine (Shenzhen Wance Experimental Equipment Co., Ltd) and compressive strength was performed by a YAW06 micro-computer-controlled pressure testing machine (Mets Industrial System Co., Ltd.). For each composition, at least five specimens were tested, whose average was regarded as the representative value of strength. The flexural strength was determined using the equation below:

$$\delta_f = 3FL / (2bd^2) \quad (1)$$

where  $\delta_f$  is flexural strength in MPa;  $F$  is maximum load in N;  $L$  is support distance in mm;  $b$  is width of the tested beam in mm and  $d$  is height of the tested beam in mm.

The compressive strength was determined using the equation below:

$$\delta_c = 4P / (\pi D^2) \quad (2)$$

where  $\delta_c$  is compressive strength in MPa;  $P$  is maximum load in N and  $D$  is diameter of the tested beam in mm.

### 2.3.2 Apparent porosity, bulk density and water absorption

The apparent porosity  $q$  (%) was calculated as follows:

$$q = \frac{m_2 - m_1}{m_2 - m_3} \times 100\% \quad (3)$$

where  $m_1$  is the mass of samples after drying in g;  $m_2$  is the mass of samples immersed in boiling water for 12 h in g and  $m_3$  is the mass of sample in water in g.

The bulk density ( $\rho$ ) was calculated as follows:

$$\rho = \frac{m}{V} \quad (4)$$

where  $m$  is the mass of samples in g and  $V$  is volume of the samples in  $\text{cm}^3$ .

The water absorption  $W_a$  (%) was calculated as follows:

$$W_a = \frac{m_4 - m_1}{m_1} \times 100\% \quad (5)$$

where  $m_4$  is the mass of samples after water absorption in g.

## 2.4 Adsorption studies

### 2.4.1 Adsorption rate and adsorption capacity

The calculation formula of adsorption rate and adsorption capacity were determined using

$$R = \frac{C_0 - C_e}{C_0} \times 100\% \quad (6)$$

$$q_e = \frac{(C_0 - C_e)V'}{m'} \quad (7)$$

where  $R$  is adsorption rate;  $C_0$  is initial concentration of MB in solution in mg/L;  $C_e$  is equilibrium concentration of MB in solution in mg/L;  $q_e$  is adsorption capacity of adsorbent in mg/g;  $V'$  is volume of MB solution in L;  $m'$  is mass of adsorbent in g.

#### 2.4.2 Pseudo-first-order and pseudo-second-order kinetic model

Pseudo-first-order equation [33] was described as follows:

$$\ln(Q_e - Q_t) = \ln Q_e - k_1 t \quad (8)$$

where  $Q_t$  (mg/g) and  $Q_e$  (mg/g) are the adsorption capacities of adsorbent towards dye solution at different contact time ( $t$ ) and equilibrium, respectively, and  $k_1$  ( $\text{min}^{-1}$ ) is the constant of pseudo-first-order rate.

Pseudo-second-order equation was described as follows:

$$\frac{t}{Q_t} = \frac{t}{k_2 Q_e^2} + \frac{t}{Q_e} \quad (9)$$

where  $k_2$  ( $\text{g}/(\text{mg} \cdot \text{min})$ ) is the constant of pseudo-second-order rate.

#### 2.4.3 Freundlich and Langmuir isotherm

The well-known expression of Freundlich isotherm model was presented as

$$Q_e = K_F C_e^{1/n} \quad (10)$$

where  $K_F$  [ $(\text{mg}/\text{g}) \cdot (\text{L}/\text{mg})^{1/n}$ ] is the adsorption equilibrium constant of Freundlich isotherm model and  $n$  is the Freundlich constant giving an indication of how favourable the adsorption process is.

The equation of Langmuir isotherm was represented as

$$Q_e = \frac{Q_m K_L C_e}{1 + K_L C_e} \quad (11)$$

where  $Q_m$  (mg/g) is the maximum theoretical adsorption capacity of adsorbent and  $K_L$  (L/mg) is the constant of Langmuir isotherm.

### 2.5 Phase composition and chemical composition

The chemical composition was examined through an Axios X-ray fluorescence (XRF) spectrometer (PANalytical B. V). The phase composition of powdered material was examined through a D/max IIIA X-ray diffractometer (XRD).

### 2.6 Scanning electron microscopy (SEM)

The samples were coated with carbon and examined through a scanning electron microscopy (SEM; LEO440, Leica Cambridge Ltd.).

### 2.7 Thermal analysis

Thermogravimetric analysis (TGA) and differential scanning calorimetry (DSC) were simultaneously performed in air through a comprehensive thermal analyser (Jupiter STA449C, Netzsch) at a constant heating rate of 20 °C/min. The samples were heated from room temperature to 800 °C.

### 2.8 FTIR analysis

Fourier transform infrared spectrometer (FTIR) produced by Perkin Elmer Instruments Co., Ltd. (USA) was used to test the samples. The medium was potassium bromide (KBr).

## 3 Design of orthogonal experiment

### 3.1 Test indicators

The flexural strength, compressive strength, apparent porosity, bulk density and water absorption were considered as optimization parameters.

### 3.2 Optimal levels of parameters

The orthogonal experimental scheme is presented in Table 2, where W-LPG, M-HP and ST respectively represent the mass ratio of LPG, hydrogen peroxide dosage and sintering temperature.

**Table 2** Factors and levels of orthogonal experiment

Factor	Level		
	1	2	3
W-LPG/wt.%	20	25	30
M-HP/(mL·kg <sup>-1</sup> )	5	10	15
ST/°C	550	600	650

### 3.3 Orthogonal experiment table

$L_9(3^3)$  was employed in the study regardless of the interactions. The actual test scheme in this work is presented in Table 3. The mass fractions of kaolin and CMC-Na were 9.5% and 0.5%. The amount of distilled water was 2.4–2.9 mL/kg.

**Table 3**  $L_9(3^3)$  orthogonal experimental scheme

Sample	W-LPG/wt.%	M-HP/(mL·kg <sup>-1</sup> )	ST/°C
S <sub>1</sub>	15	5	550
S <sub>2</sub>	15	10	600
S <sub>3</sub>	15	15	650
S <sub>4</sub>	20	5	600
S <sub>5</sub>	20	10	650
S <sub>6</sub>	20	15	550
S <sub>7</sub>	25	5	650
S <sub>8</sub>	25	10	550
S <sub>9</sub>	25	15	600

## 4 Results and discussion

### 4.1 Macroscopic appearances of porous ceramic materials and LPG

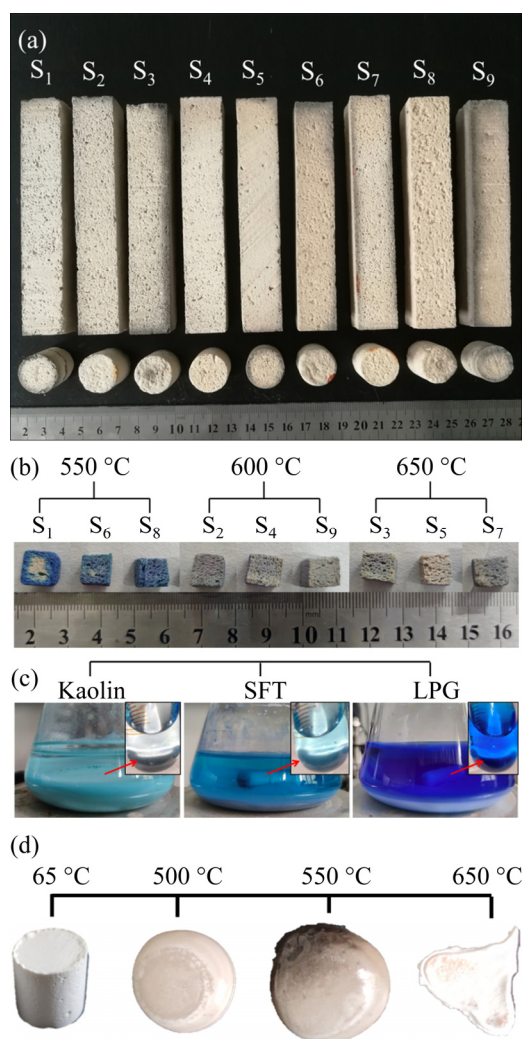
The appearances of porous ceramics are presented in Fig. 2(a) and the section morphologies of porous ceramics after adsorption of MB are presented in Fig. 2(b). However, it is more difficult to cut and quantify the bulk sample than the powder, so the samples were ground to powder to compare their adsorption performance more conveniently and accurately.

Figure 2(c) represents that kaolin had the best adsorption performance compared with SFT and LPG. The dosage of powder, stirring time, concentration of MB and volume of solution were 10 g, 2 h, 25 mg/L and 200 mL, respectively. The appearance morphologies of LPG at different sintering temperatures are presented in Fig. 2(d). LPG softened obviously at the sintering temperature of 550 °C and the softening phenomenon was intensified with the rise of sintering temperature, which could be the main reason for the tight bonding among ceramic particles.

### 4.2 Orthogonal analysis of various influencing factors on physical properties

#### 4.2.1 Results of physical properties

Physical properties of porous ceramics are presented in Table 4. The average values of flexural strength, compressive strength, apparent porosity, water absorption and bulk density were 5.60 MPa, 4.66 MPa, 52.27%, 44.32% and 1.20 g/cm<sup>3</sup>, respectively.



**Fig. 2** Appearances of porous ceramics (a), section morphologies of porous ceramics with adsorption of MB (b), appearances of MB solution after adsorption of raw materials (c) and morphologies of LPG at different sintering temperatures (d)

#### 4.2.2 Range analysis of various factors

$K_i$  ( $i=1, 2, 3$ ) is defined as the average value of the evaluation indexes at three levels in each factor.  $R_j$  ( $j$  represents different result parameters) is defined as the range between the maximum and minimum  $K$  value in the column of the corresponding factor. Range  $R_j$  reflects the influence degree of each factor on the physical properties of porous ceramics and the larger range indicates that the impact of indicators is greater [34].  $R_F$  and  $R_C$  in Table 5 were the highest values in the position of ST (2.71 and 1.73, respectively), which means that the flexural strength and the compressive strength of porous ceramics were more affected by sintering temperature. A higher sintering temperature would

**Table 4** Physical properties of porous ceramics

Sample	Flexural strength/MPa	Compressive strength/MPa	Apparent porosity/%	Water absorption/%	Bulk density/(g·cm <sup>-3</sup> )
S <sub>1</sub>	3.89	4.02	51.42	41.09	1.25
S <sub>2</sub>	5.19	4.25	53.71	45.27	1.19
S <sub>3</sub>	5.29	4.22	56.79	51.36	1.11
S <sub>4</sub>	6.09	4.47	50.65	40.35	1.26
S <sub>5</sub>	6.23	5.04	54.49	47.37	1.15
S <sub>6</sub>	4.67	3.44	56.71	52.68	1.08
S <sub>7</sub>	9.32	7.20	38.27	26.05	1.47
S <sub>8</sub>	4.16	3.83	56.05	50.59	1.11
S <sub>9</sub>	5.53	5.46	52.33	44.12	1.19
Mean	5.60	4.66	52.27	44.32	1.20

**Table 5** Range analysis of orthogonal experiment results

Parameter	$K_i, R_j$	W-LPG/ wt.%	M-HP/ (mL·kg <sup>-1</sup> )	ST/ °C
Flexural strength	$K_1$	4.79	6.43	4.24
	$K_2$	5.66	5.19	5.60
	$K_3$	6.34	5.16	6.95
	$R_F$	1.55	1.27	2.71
Compressive strength	$K_1$	4.17	5.23	3.76
	$K_2$	4.32	4.38	4.73
	$K_3$	5.50	4.37	5.49
	$R_C$	1.33	0.86	1.73
Apparent porosity	$K_1$	53.97	46.78	54.73
	$K_2$	53.95	54.75	52.23
	$K_3$	48.88	55.27	49.85
	$R_A$	5.09	8.50	4.87
Water adsorption	$K_1$	45.91	35.83	48.12
	$K_2$	46.80	47.74	43.25
	$K_3$	40.25	49.38	41.59
	$R_W$	6.55	13.55	6.53
Bulk density	$K_1$	1.18	1.33	1.15
	$K_2$	1.16	1.15	1.21
	$K_3$	1.25	1.12	1.24
	$R_B$	0.09	0.20	0.10

ultimately enhance the mass transfer among particles, which might develop the flexural strength and compressive strength of ceramics eventually. On the other hand, the apparent porosity, water absorption and bulk density of porous

ceramics were more affected by the dosage of H<sub>2</sub>O<sub>2</sub>.

#### 4.2.3 Trend analysis of various influencing factors

The influential trends of various factors on the properties of porous ceramic materials are presented in Fig. 3 and Fig. 4. With the rise of sintering temperature, the flexural strength and compressive strength of porous ceramics were gradually increased. The enhancement of mass transfer among particles and the intensification of the softening of LPG might be the main reasons.

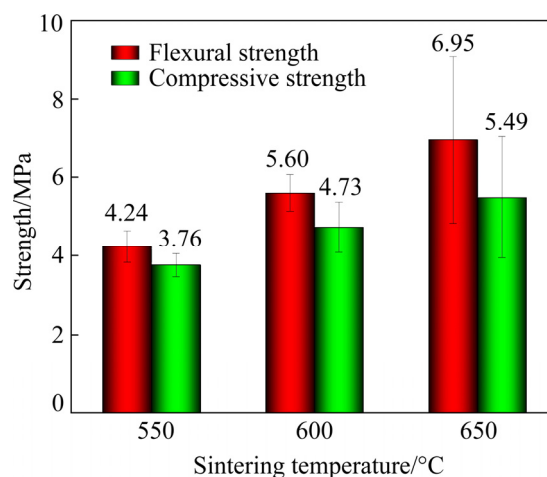


**Fig. 3** Effect of sintering temperature on flexural strength and compressive strength of porous ceramics

Figure 4 presents that apparent porosity and water absorption of porous ceramics increased with the increase of H<sub>2</sub>O<sub>2</sub> dosage. This was because more H<sub>2</sub>O<sub>2</sub> participated in the chemical reaction and more gas was produced, which increased the porosity of porous ceramics.

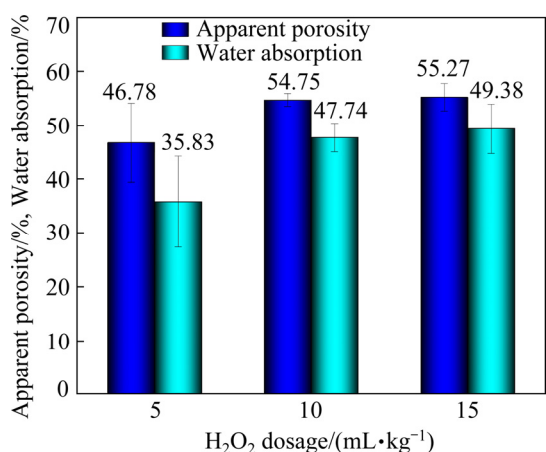


**Fig. 4** Effect of H<sub>2</sub>O<sub>2</sub> dosage on apparent porosity and water absorption of porous ceramics

### 4.3 Analysis on adsorption properties of porous ceramic powder

#### 4.3.1 Effect of adsorption time on properties of porous ceramics

Figures 5(a, b) represent the effect of adsorption time on the adsorption capacity of porous

ceramics and the removal rate of MB. The adsorption properties decreased significantly with the increase of sintering temperature. The adsorption capacity and adsorption rate of porous ceramics did not change significantly after 2 h, which indicates that the adsorption equilibrium was basically reached after 2 h. Therefore, Samples S<sub>1</sub>, S<sub>2</sub> and S<sub>3</sub> with the highest adsorption capacity at the same sintering temperature were selected to further test their adsorption performance, whose adsorption time was 2 h.

#### 4.3.2 Effect of porous ceramic powder dosage on MB adsorption

The results of adsorption isotherm of three samples at the sintering temperature of 550 °C (Sample S<sub>1</sub>), 600 °C (Sample S<sub>2</sub>) and 650 °C (Sample S<sub>3</sub>) are presented in Fig. 6.  $Q_e$  decreased and the removal rate increased gradually with an increased dosage of samples. Sample S<sub>1</sub> was selected for the test on adsorption kinetics because of its best adsorption performance.

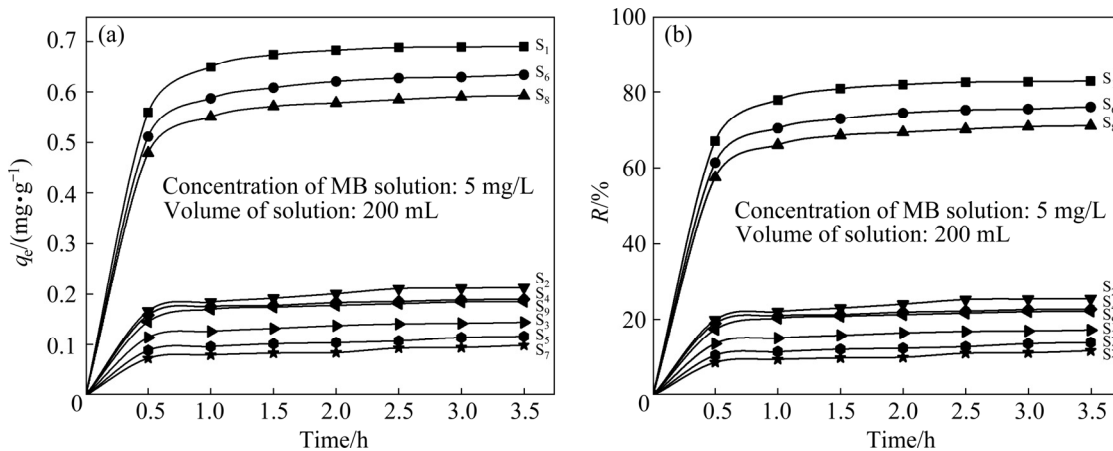


**Fig. 5** Effect of adsorption time on adsorption capacity of porous ceramics (a) and removal rate of MB (b)

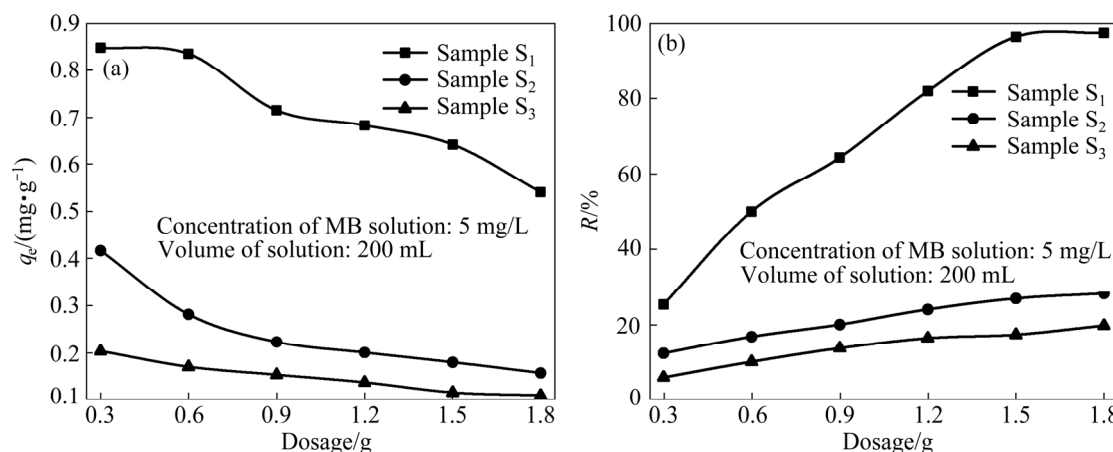


**Fig. 6** Effect of porous ceramics dosage on adsorption capacity (a) and removal rate (b) of MB

### 4.3.3 Adsorption kinetics analysis

Commonly, pseudo-first-order and pseudo-second-order kinetic models [35] are used to analyze the adsorption process, as shown in Fig. 7. Kinetic parameters including correlation coefficients ( $R^2$ ),  $k_1$ ,  $k_2$  and the calculated  $Q_e$  are displayed in Table 6. Obviously, the pseudo-second-order kinetic model for the adsorption of Sample S<sub>1</sub> represented a better regression coefficient of the kinetic data ( $R^2=0.985$ ) compared to pseudo-first-order kinetic model ( $R^2=0.961$ ). Based on the assumption of pseudo-second-order kinetic model [36], it was inferred that the adsorption mechanism of MB from porous ceramics might be a chemical reaction [33,37].

### 4.3.4 Adsorption isotherms

Adsorption isotherms, especially the two common isotherm models, namely Freundlich and Langmuir isotherm, play important roles in depicting the interaction pathways to solid-solution adsorption system [33,35]. The fitted curves of Langmuir and Freundlich isotherm are presented in

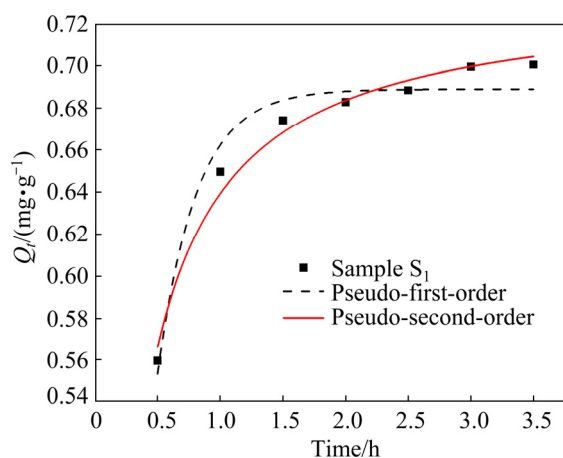


Fig. 7 Fitted kinetic models based on experimental data

Table 6 Kinetic parameters for adsorption of MB onto porous ceramic powder (Sample S<sub>1</sub>)

Pseudo-first-order			Pseudo-second-order		
$Q_{e(cal)}/$ ( $mg \cdot g^{-1}$ )	$k_1/$ $h^{-1}$	$R^2$	$Q_{e(cal)}/$ ( $mg \cdot g^{-1}$ )	$k_2/$ ( $g \cdot mg^{-1} \cdot h^{-1}$ )	$R^2$
0.685	-3.25	0.961	0.727	9.17	0.985

Table 7 Parameters of adsorption isotherm of MB onto porous ceramic powder (Sample S<sub>1</sub>)

Freundlich model			Langmuir model		
$K_F/[(mg \cdot g^{-1}) \cdot (L \cdot mg^{-1})^{1/n}]$	$1/n$	$R^2$	$Q_m/(mg \cdot g^{-1})$	$K_L/(L \cdot mg^{-1})$	$R^2$
0.734	0.11	0.920	0.823	16.17	0.968

Fig. 8. Table 7 represents the correlation coefficient of these two fitted models. It can be seen that the experimental data were better fitted by the Langmuir isotherm model ( $R^2=0.968$ ). On the other hand, calculated  $Q_m$  value of Langmuir isotherm model for Sample S<sub>1</sub> (0.823 mg/g) was closer to the corresponding experimental data (0.822 mg/g) and  $1/n$  was between 1 and 2, which means that the adsorption was favourable [38,39].

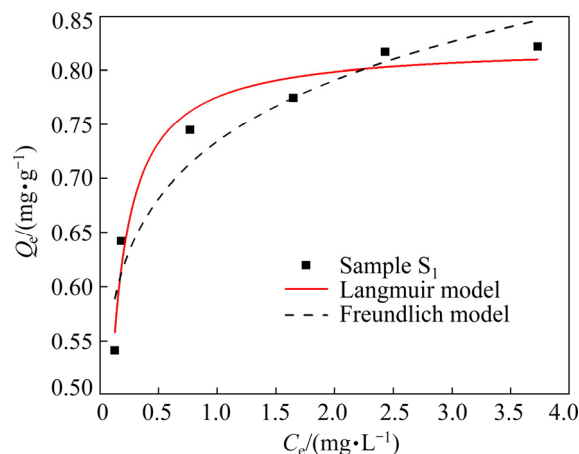


Fig. 8 Fitted models from experimental data

## 4.4 Phase composition

Figure 9 presents the phase composition of the green materials and samples. Quartz ( $SiO_2$ , PDF # 46-1045), muscovite ( $KAl_2(AlSi_3O_{10})(OH)_2$ , PDF # 07-0042), albite ( $Na_2O \cdot Al_2O_3 \cdot 6SiO_2$ , PDF #09-0466) and microcline ( $KAlSi_3O_8$ , PDF #19-0932) were main phase compositions of SFT. The diffraction peak of LPG powder was diffused, which was a typical feature of glass diffraction and there was no obvious crystallization peak in the sample [12,40,41]. Quartz, albite, muscovite and microcline were the main components of the sintered samples (S<sub>1</sub>, S<sub>2</sub>, S<sub>3</sub>) with similar XRD patterns.

Figure 9(b) presents that the kaolinite ( $Al_2Si_2O_5(OH)_4$ , PDF #14-0164) was the main phase composition of kaolin. The peak of kaolinite gradually disappeared with the rise of sintering temperature, which was due to the dehydration and decomposition of kaolinite at 600 °C when

amorphous metakaolin was formed. It might be the main reason for the decrease of adsorption properties of porous ceramics with increasing the sintering temperature.

#### 4.5 SEM analysis results

The SEM images of the samples are presented in Fig. 10. Figures 10(a, d, g) represent that the sample was fused into a unified whole and it was proven that the particles were closely bonded, which might be attributed to the softening of LPG powder that filled the gap among particles and made them adhere to each other closely. Mass

transfer among particles was enhanced with the rise of sintering temperature and the pores among them gradually decreased and shrank. The layered material in Figs. 10(b, c, e, h) was speculated to muscovite, which might influence the mechanical property of porous ceramics.

Figures 11(a–i) present the results of EDS mappings of porous ceramics (Sample S<sub>1</sub>) before adsorption of MB and Figs. 11(j–r) represent the results of porous ceramics after adsorption of MB. Figs. 11(a–c, j–l) present that P and Na elements were mainly distributed around the large particles in the white oval box, which were the main elements

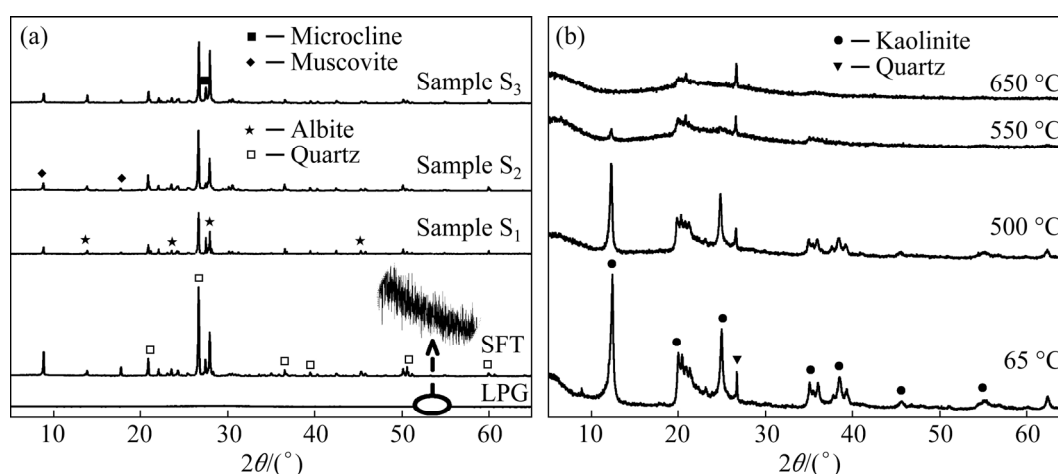


**Fig. 9** XRD patterns of samples at different sintering temperatures: (a) SFT and porous ceramics; (b) Kaolin

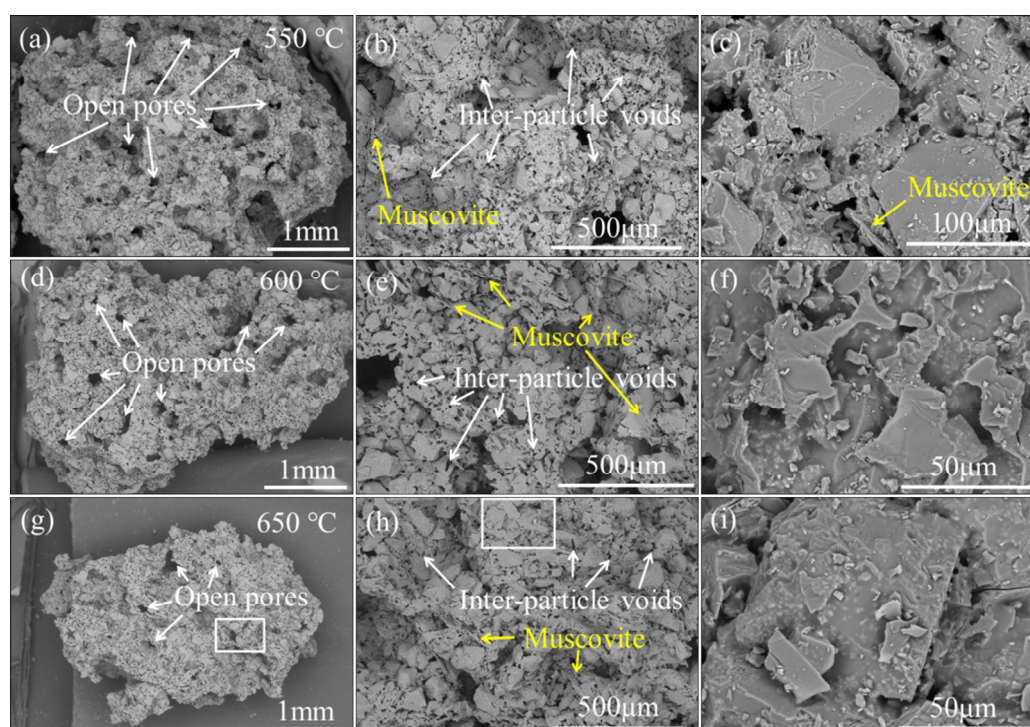


**Fig. 10** SEM images of samples at different sintering temperatures: (a–c) 550 °C; (b–f) 600 °C; (g–i) 650 °C

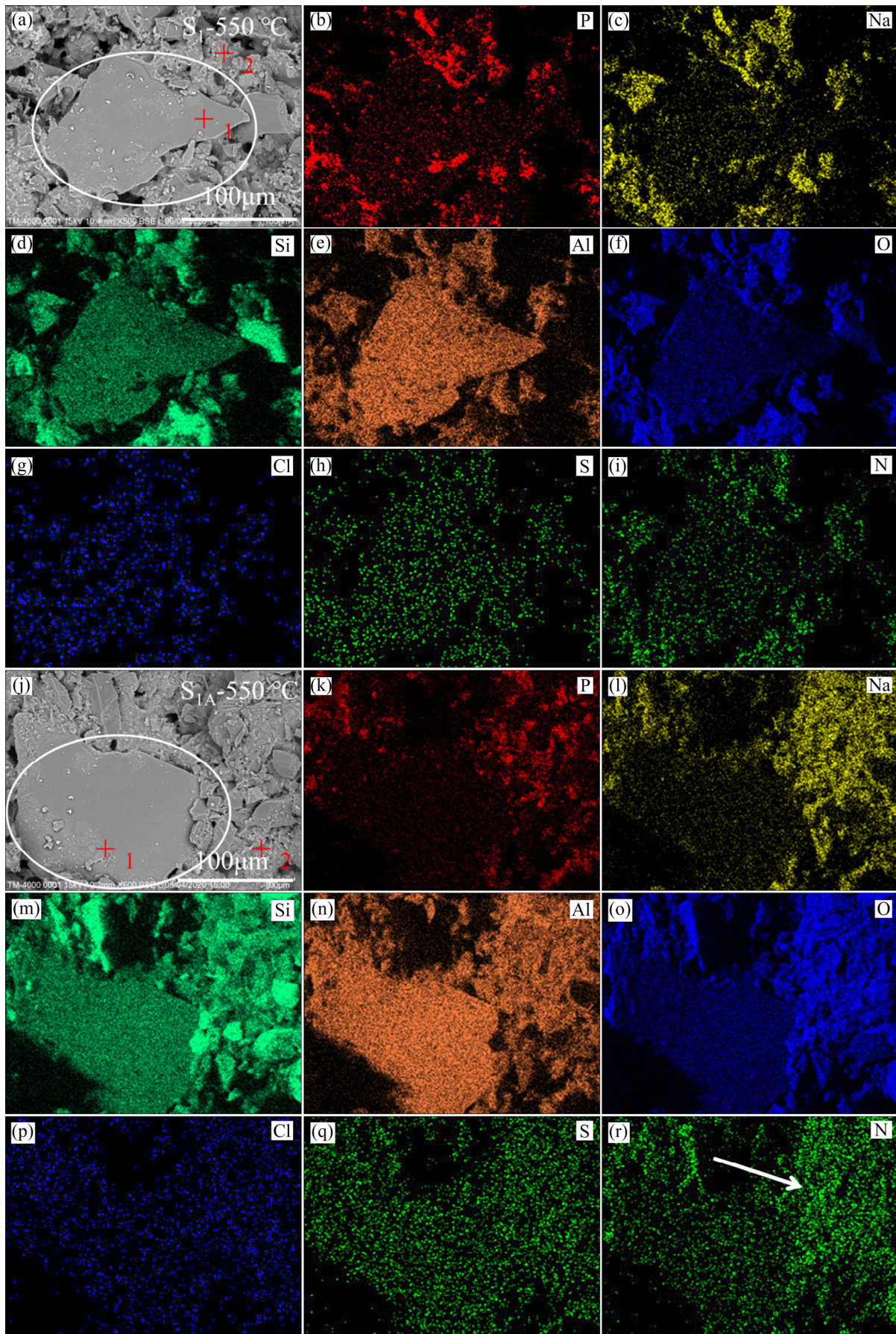


**Fig. 11** EDS mapping results of Sample S<sub>1</sub>: (a–i) Before adsorption of MB; (j–r) After adsorption of MB

of LPG. Si and Al were concentrated on large particles, which were the main components of SFT (Figs. 11(d, e, m, n)). Figures 11(p–r) present that there were more Cl, S and N elements on the surface of the sample after adsorption of MB, which indicated that MB was successfully adsorbed on porous ceramics. Figure 11(r) represents that N was mainly concentrated around mineral particles, which indicated that the adsorption property of mineral particles might be poor.

#### 4.6 TGA–DSC test results

TGA–DSC results of SFT and kaolin are presented in Fig. 12, which presents that the total mass loss of SFT was low until 800 °C. An exothermic peak appeared at 350 °C and accompanied by the decrease of mass fraction, which was likely due to the dehydration of intergranular water. A sharp exothermic peak appeared at 572 °C, which was due to the rapid transformation of  $\beta$ -quartz and  $\alpha$ -quartz [16]. There was a huge exothermic peak at 525 °C, where the mass fraction of kaolin decreases significantly

(10.5%), which was due to the kaolin converting to metakaolin (450–600 °C) [42–44]. This might be the main reason for the decrease of adsorption properties of porous ceramics with the increase of sintering temperature.

#### 4.7 FT–IR analysis results

FT–IR spectroscopy of SFT, kaolin and Samples S<sub>1</sub>, S<sub>2</sub> and S<sub>3</sub> are presented in Fig. 13. Bands of kaolin at 3691 and 3619 cm<sup>-1</sup> were assigned to the stretch vibration of Si–OH or Al–OH hydroxyl group, which were typical peaks of inner and outer hydroxyl groups of kaolin [45–47]. The absorption peak at 3438 cm<sup>-1</sup> was attributed to O–H stretching vibration of water [48,49]. The peak at 1140 cm<sup>-1</sup> was attributed to the stretch of Si–O, which was weakened with the rise of sintering temperature. This might be due to the destruction of the crystal structure of kaolin and the formation of metakaolin through dehydration reaction [50]. The spectrum presented a stronger absorption band at 2971 and 2920 cm<sup>-1</sup>, which were assigned to the C–H stretching band

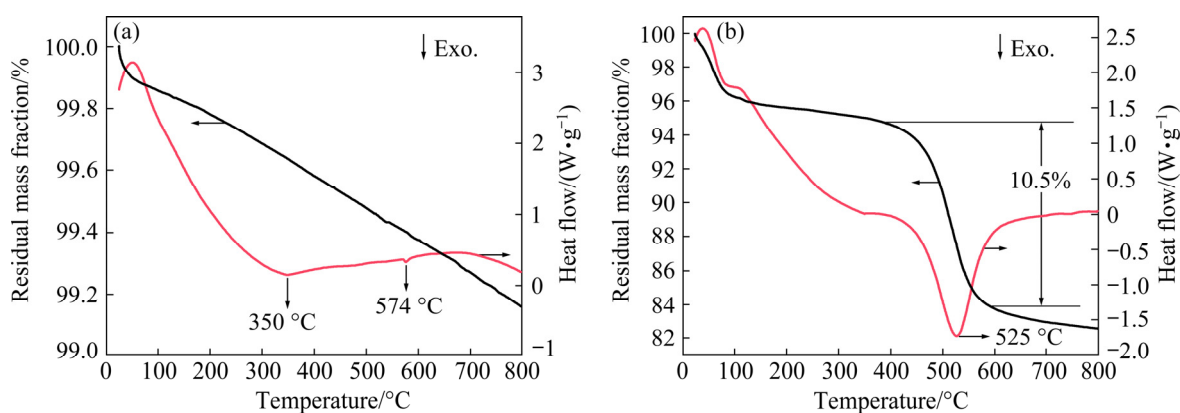


Fig. 12 TGA–DSC curves of SFT (a) and Kaolin (b)

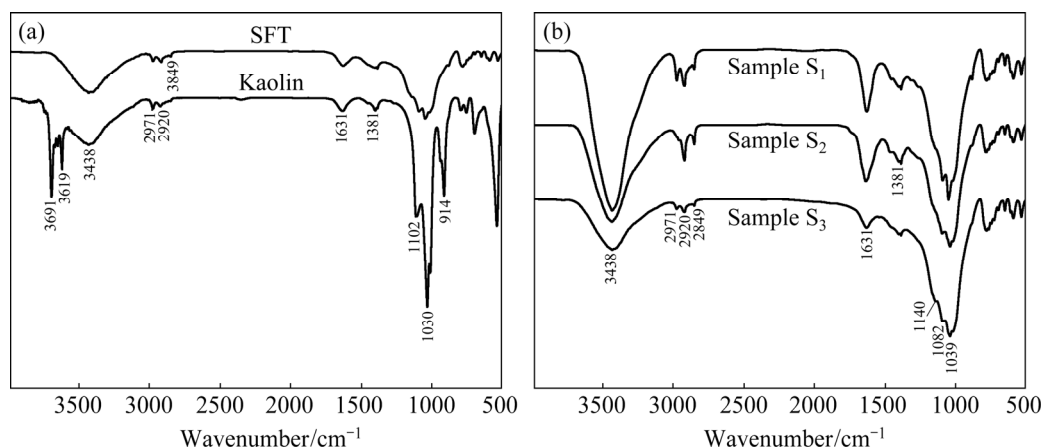


Fig. 13 FT–IR spectra of samples: (a) Kaolin and SFT; (b) Samples S<sub>1</sub>, S<sub>2</sub> and S<sub>3</sub>

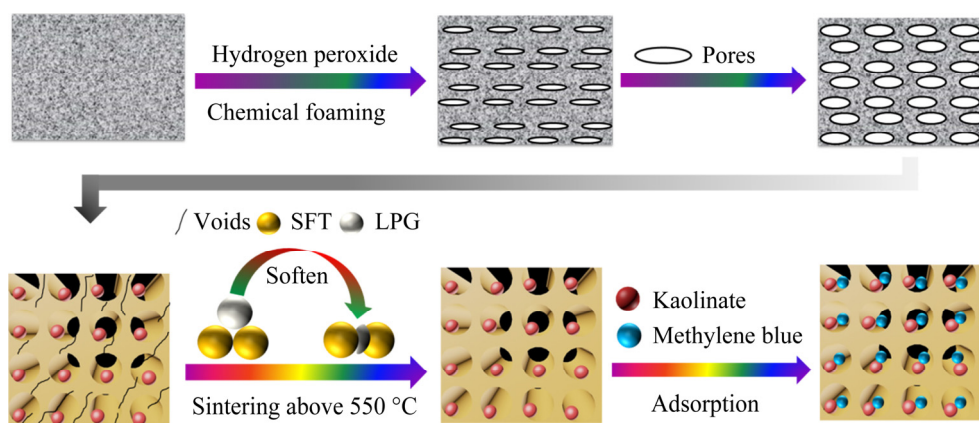


Fig. 14 Schematic diagram of mechanism

of the  $-\text{CH}_3$  and  $-\text{CH}_2$  groups [51]. The presence of the band at  $1631\text{ cm}^{-1}$  was for the stretching of  $-\text{OH}$  [52]. The absorption band at  $1381\text{ cm}^{-1}$  was attributed to the deformation vibration of water molecules [46]. Peaks of  $1000\text{--}1100$  ( $\text{Si}-\text{O}$  stretch) and  $900\text{--}950\text{ cm}^{-1}$  ( $\text{Al}-\text{OH}$  vibration) were typical features of kaolin clay [32,53].

#### 4.8 Mechanism

The mechanism could be divided into three processes: foaming process, sintering process and adsorption process. In the foaming process, the addition of  $\text{H}_2\text{O}_2$  produced a large amount of pores and the accumulation of mineral particles also created some pores. The porous structure increased the contact area of the ceramics with contaminants in the water. The main sintering mechanism at a lower temperature was a result of the softening of LPG, which made particles bonded as a whole and the sintering temperature was reduced to a range where kaolinite still had a good adsorption performance, as shown in Fig. 14.

### 5 Conclusions

(1) Porous ceramics were successfully prepared through  $\text{H}_2\text{O}_2$  foaming method and the sintering temperature was reduced with the addition of LPG. The tailings had a high utilization rate (up to 80%), a high apparent porosity and water absorption (52.27% and 44.32% on average) as well as good mechanical properties (average flexural strength and compressive strength of 5.60 MPa and 4.66 MPa, respectively). The maximum adsorption

capacity of porous ceramics to MB was about 0.7 mg/g.

(2) The flexural strength and compressive strength of porous ceramic materials were greatly influenced by the sintering temperature, which had a positive correlation between them. The apparent porosity and water absorption of porous ceramics were greatly determined by the dosage of  $\text{H}_2\text{O}_2$ , which had a positive correlation, too.

(3) The flowing liquid phase of LPG filled the gaps among the particles, and made them adhere to each other, which was the main reason for the improvement of mechanical properties of porous ceramics. The reason why the adsorption performance declined with the rise of sintering temperature was that kaolinite was gradually changed into metakaolin.

### Acknowledgments

The authors are grateful for the financial supports from the National Natural Science Foundation of China (Nos. 51674207, 51922091), the Young Elite Scientists Sponsorship Program by CAST, China (No. 2018QNR001), and the Sichuan Science and Technology Program, China (Nos. 2019YFS0453, 2018JY0148).

### References

- [1] COSTA C M, LEE Y H, KIM J H, LEE S Y, LANCEROS-MÉNDEZ S. Recent advances on separator membranes for lithium-ion battery applications: From porous membranes to solid electrolytes [J]. *Energy Storage Materials*, 2019, 22: 346–375.
- [2] HANNAN M A, LIPU M S H, HUSSAIN A, MOHAMED A.

- A review of lithium-ion battery state of charge estimation and management system in electric vehicle applications: Challenges and recommendations [J]. *Renewable and Sustainable Energy Reviews*, 2017, 78: 834–854.
- [3] XIONG Rui, PAN Yue, SHEN Wei-xiang, LI Hai-long, SUN Feng-chun. Lithium-ion battery aging mechanisms and diagnosis method for automotive applications: Recent advances and perspectives [J]. *Renewable and Sustainable Energy Reviews*, 2020, 131: 110048.
- [4] TIAN Jia, XU Long-hua, DENG Wei, JIANG Hao, GAO Zhi-yong, HU Yue-hua. Adsorption mechanism of new mixed anionic/cationic collectors in a spodumene–feldspar flotation system [J]. *Chemical Engineering Science*, 2017, 164: 99–107.
- [5] TIAN Jia, XU Long-hua, WU Hou-qin, FANG Shuai, DENG Wei, PENG Tie-feng, SUN Wei, HU Yue-hua. A novel approach for flotation recovery of spodumene, mica and feldspar from a lithium pegmatite ore [J]. *Journal of Cleaner Production*, 2018, 174: 625–633.
- [6] WU Hou-qin, TIAN Jia, XU Long-hua, FANG Shuai, ZHANG Zhen-yue, CHI Ruan. Flotation and adsorption of a new mixed anionic/cationic collector in the spodumene–feldspar system [J]. *Minerals Engineering*, 2018, 127: 42–47.
- [7] XU Long-hua, PENG Tie-feng, TIAN Jia, LU Zhong-yuan, HU Yue-hua, SUN Wei. Anisotropic surface physicochemical properties of spodumene and albite crystals: Implications for flotation separation [J]. *Applied Surface Science*, 2017, 426: 1005–1022.
- [8] KARHU M, LAGERBOM J, SOLISMAA S, HONKANEN M, ISMAILOV A, RÄISÄNEN M L, HUTTUNEN-SAAIRIVIRTA E, LEVÄNEN E, KIVIKYTÖ-REPONEN P. Mining tailings as raw materials for reaction-sintered aluminosilicate ceramics: Effect of mineralogical composition on microstructure and properties [J]. *Ceramics International*, 2019, 45(4): 4840–4848.
- [9] EGLI M, BERGER A, KÜNDIG R, KREBS R, de CASTRO PORTES R, BERGER R, WIDMER R. The long-term interaction of mine tailings with soils and the wider environment: Examples from Mont Chemin, Switzerland [J]. *Journal of Geochemical Exploration*, 2017, 182: 53–69.
- [10] SAEDI A, JAMSHIDI-ZANJANI A, DARBAN A K. A review on different methods of activating tailings to improve their cementitious property as cemented paste and reusability [J]. *Journal of Environmental Management*, 2020, 270: 110881.
- [11] XI Cui-ping, ZHOU Jian-min, ZHENG Feng, GAO Jian-ming, HU Peng-fei, LI Yang, ZHEN Qiang, BASHIR S, LIU J L. Conversion of extracted titanium tailing and waste glass to value-added porous glass ceramic with improved performances [J]. *Journal of Environmental Management*, 2020, 261: 110197.
- [12] ZENG Li, SUN Hong-juan, PENG Tong-jiang, ZHENG Wen-miao. Preparation of porous glass-ceramics from coal fly ash and asbestos tailings by high-temperature pore-forming [J]. *Waste Management*, 2020, 106: 184–192.
- [13] LEMOUGNA P N, YLINIEMI J, ADESANYA E, TANSKANEN P, KINNUNEN P, RONG J, ILLIKAINEN M. Reuse of copper slag in high-strength building ceramics containing spodumene tailings as fluxing agent [J]. *Minerals Engineering*, 2020, 155: 106448.
- [14] LEMOUGNA P N, YLINIEMI J, ISMAILOV A, LEVANEN E, TANSKANEN P, KINNUNEN P, RONG J, ILLIKAINEN M. Recycling lithium mine tailings in the production of low temperature (700–900 °C) ceramics: Effect of ladle slag and sodium compounds on the processing and final properties [J]. *Construction and Building Materials*, 2019, 221: 332–344.
- [15] LEMOUGNA P N, YLINIEMI J, ISMAILOV A, LEVANEN E, TANSKANEN P, KINNUNEN P, RONG J, ILLIKAINEN M. Spodumene tailings for porcelain and structural materials: Effect of temperature (1050–1200 °C) on the sintering and properties [J]. *Minerals Engineering*, 2019, 141: 105843.
- [16] LEMOUGNA P N, YLINIEMI J, NGUYEN H, ADESANYA E, TANSKANEN P, KINNUNEN P, RONG J, ILLIKAINEN M. Utilisation of glass wool waste and mine tailings in high performance building ceramics [J]. *Journal of Building Engineering*, 2020, 31: 101383.
- [17] HU Jian-hua, REN Qi-fan, YANG Dong-jie, MA Shao-wei, SHANG Jun-long, DING Xiao-tian, LUO Zhou-quan. Cross-scale characteristics of backfill material using NMR and fractal theory [J]. *Transactions of Nonferrous Metals Society of China*, 2020, 30(5): 1347–1363.
- [18] ALQADAMI A A, NAUSHAD M, ALOTHMAN Z A, AHAMAD T. Adsorptive performance of MOF nanocomposite for MB and malachite green dyes: Kinetics, isotherm and mechanism [J]. *Journal of Environmental Management*, 2018, 223: 29–36.
- [19] MOHANRAJ J, DURGALAKSHMI D, BALAKUMAR S, ARUNA P, GANESAN S, RAJENDRAN S, NAUSHAD M. Low cost and quick time absorption of organic dye pollutants under ambient condition using partially exfoliated graphite [J]. *Journal of Water Process Engineering*, 2020, 34: 101078.
- [20] GAN Wei, SHANG Xin, LI Xuan-Hua, ZHANG Jian, FU Xu-cheng. Achieving high adsorption capacity and ultrafast removal of methylene blue and Pb<sup>2+</sup> by graphene-like TiO<sub>2</sub>@C [J]. *Colloids and Surfaces A: Physicochemical and Engineering Aspects*, 2019, 561: 218–225.
- [21] CHENG Li-yuan, LIU Hong, CUI Yu-ming, XUE Nian-hua, DING Wei-ping. Direct conversion of corn cob to formic and acetic acids over nano oxide catalysts [J]. *Journal of Energy Chemistry*, 2014, 23(1): 43–49.
- [22] HUANG Yun-zhu, SUI Qian, LYU Shu-guang, WANG Jia-qi, HUANG Shao-xin, ZHAO Wen-tao, WANG Bin, XU Dong-jiong, KONG Ming, ZHANG Yi-min, YU Gang. Tracking emission sources of PAHs in a region with pollution-intensive industries, Taihu Basin: From potential pollution sources to surface water [J]. *Environmental Pollution*, 2020, 264: 114674.
- [23] KUMAR P, LIU Wei, CHU Xi, ZHANG Yue, LI Zhi-hui. Integrated water resources management for an inland river basin in China [J]. *Watershed Ecology and the Environment*, 2019, 1: 33–38.
- [24] WANG Jin-xia, LI Yan-rong, HUANG Ji-kun, YAN Ting-ting, SUN Tian-he. Growing water scarcity, food security and government responses in China [J]. *Global Food Security*, 2017, 14: 9–17.
- [25] MOUNI L, BELKHIRI L, BOLLINGER J C, BOUZAZA A,

- ASSADI A, TIRRI A, DAHMOUNE F, MADANI K, REMINI H. Removal of methylene blue from aqueous solutions by adsorption on kaolin: Kinetic and equilibrium studies [J]. *Applied Clay Science*, 2018, 153: 38–45.
- [26] SANTOSO E, EDIATI R, KUSUMAWATI Y, BAHRUJI H, SULISTIONO DO, PRASETYOKO D. Review on recent advances of carbon based adsorbent for methylene blue removal from waste water [J]. *Materials Today Chemistry*, 2020, 16: 100233.
- [27] HAN Qiao-ning, WANG Jing, GOODMAN B A, XIE Jun-kang, LIU Zu-guang. High adsorption of methylene blue by activated carbon prepared from phosphoric acid treated eucalyptus residue [J]. *Powder Technology*, 2020, 366: 239–248.
- [28] ÜNER O. Hydrogen storage capacity and methylene blue adsorption performance of activated carbon produced from *Arundo donax* [J]. *Materials Chemistry and Physics*, 2019, 237: 121858.
- [29] DENG Wei-jie, TANG Shu-wei, ZHOU Xi, LIU Ye, LIU Shi-jie, LUO Ji-wen. Honeycomb-like structure-tunable chitosan-based porous carbon microspheres for methylene blue efficient removal [J]. *Carbohydrate Polymers*, 2020, 247: 116736.
- [30] SABAR S, ABDUL AZIZ H, YUSOF N H, SUBRAMANIAM S, FOO K Y, WILSON L D, LEE H K. Preparation of sulfonated chitosan for enhanced adsorption of methylene blue from aqueous solution [J]. *Reactive and Functional Polymers*, 2020, 151: 104584.
- [31] RIDA K, BOURAOUI S, HADNINE S. Adsorption of methylene blue from aqueous solution by kaolin and zeolite [J]. *Applied Clay Science*, 2013, 83–84: 99–105.
- [32] YAVUZ Ö, SAKA C. Surface modification with cold plasma application on kaolin and its effects on the adsorption of methylene blue [J]. *Applied Clay Science*, 2013, 85: 96–102.
- [33] HE Kai, ZENG Guang-ming, CHEN An-wei, HUANG Zhen-zhen, PENG Min, HUANG Tian-tian, CHEN Gui-qiu. Graphene hybridized polydopamine-kaolin composite as effective adsorbent for methylene blue removal [J]. *Composites Part B: Engineering*, 2019, 161: 141–149.
- [34] DENG Li-na, FENG Bo, ZHANG Yue. An optimization method for multi-objective and multi-factor designing of a ceramic slurry: Combining orthogonal experimental design with artificial neural networks [J]. *Ceramics International*, 2018, 44(13): 15918–15923.
- [35] HUANG Qiang, LIU Mei-ying, DENG Feng-jie, WANG Ke, HUANG Hong-ye, XU Da-zhuang, ZENG Guang-jian, ZHANG Xiao-yong, WEI Yen. Mussel inspired preparation of amine-functionalized kaolin for effective removal of heavy metal ions [J]. *Materials Chemistry and Physics*, 2016, 181: 116–125.
- [36] HAFEZI MOGHADDAM R, HAJI SHABANI A M, DADFARNIA S. Synthesis of new hydrogels based on pectin by electron beam irradiation with and without surface modification for methylene blue removal [J]. *Journal of Environmental Chemical Engineering*, 2019, 7(1): 102919.
- [37] LONG Fei, GONG Ji-lai, ZENG Guang-ming, CHEN Long, WANG Xi-yang, DENG Jiu-hua, NIU Qiu-ya, ZHANG Hui-ying, ZHANG Xiu-rong. Removal of phosphate from aqueous solution by magnetic Fe–Zr binary oxide [J]. *Chemical Engineering Journal*, 2011, 171(2): 448–455.
- [38] RAUF M A, BUKALLAH S B, HAMOUR F A, NASIR A S. Adsorption of dyes from aqueous solutions onto sand and their kinetic behavior [J]. *Chemical Engineering Journal*, 2008, 137(2): 238–243.
- [39] HE Kai, CHEN Gui-qiu, ZENG Guang-ming, CHEN An-wei, HUANG Zhen-zhen, SHI Jiang-bo, PENG Min, HUANG Tian-tian, HU Liang. Enhanced removal performance for methylene blue by kaolin with graphene oxide modification [J]. *Journal of the Taiwan Institute of Chemical Engineers*, 2018, 89: 77–85.
- [40] DENG L, KOSIBA K, LIMBACH R, WONDRAKZEK L, KÜHN U, PAULY S. Plastic deformation of a Zr-based bulk metallic glass fabricated by selective laser melting [J]. *Journal of Materials Science & Technology*, 2021, 60: 139–146.
- [41] WEI Wei, LIU Yong, TAN Yan-ni, GROVER L, GUO Yu, LIU Bo-wei. A mica/nepheline glass-ceramic prepared by melting and powder metallurgy at low temperatures [J]. *Materials Today Communications*, 2017, 11: 87–93.
- [42] LAO Xin-bin, XU Xiao-yang, JIANG Wei-hui, LIANG Jian, MIAO Li-feng, WU Qian. Influences of impurities and mineralogical structure of different kaolin minerals on thermal properties of cordierite ceramics for high-temperature thermal storage [J]. *Applied Clay Science*, 2020, 187: 105485.
- [43] MOHAMED SOLTAN A M, PÖHLER K, FUCHS F, EL-RAOOF F A, EL-KALIOUBY BA H, KOENIG A, PÖLLMANN H. Clay-bricks from recycled rock tailings [J]. *Ceramics International*, 2016, 42(15): 16685–16696.
- [44] BEWA C N, TCHAKOUTÉ H K, BANENZOUÉ C, CAKANOU L, MBAKOP T T, KAMSEU E, RÜSCHER C H. Acid-based geopolymers using waste fired brick and different metakaolins as raw materials [J]. *Applied Clay Science*, 2020, 198: 105813.
- [45] JAWAD A H, ABDULHAMEED A S. Mesoporous Iraqi red kaolin clay as an efficient adsorbent for methylene blue dye: Adsorption kinetic, isotherm and mechanism study [J]. *Surfaces and Interfaces*, 2020, 18: 100422.
- [46] KHAIRY M, AYOUB H A, RASHWAN F A, ABDEL-HAFEZ H F. Chemical modification of commercial kaolin for mitigation of organic pollutants in environment via adsorption and generation of inorganic pesticides [J]. *Applied Clay Science*, 2018, 153: 124–133.
- [47] KŘEPELOVÁ A, REICH T, SACHS S, DREBERT J, BERNHARD G. Structural characterization of U(VI) surface complexes on kaolinite in the presence of humic acid using EXAFS spectroscopy [J]. *Journal of Colloid and Interface Science*, 2008, 319(1): 40–47.
- [48] LI Guang-she, LI Li-ping, SMITH R L, INOMATA H. Characterization of the dispersion process for NiFe<sub>2</sub>O<sub>4</sub> nanocrystals in a silica matrix with infrared spectroscopy and electron paramagnetic resonance [J]. *Journal of Molecular Structure*, 2001, 560(1): 87–93.
- [49] JIN Jiao, GAO Yu-chao, WU Yin-rui, LI Rui, LIU Ruo-hua, WEI Hui, QIAN Guo-ping, ZHENG Jian-long. Performance evaluation of surface-organic grafting on the palygorskite nanofiber for the modification of asphalt [J]. *Construction*

- and Building Materials, 2020: 121072.
- [50] CHANDRASEKHAR S, PRAMADA P N. Kaolin-based zeolite Y, a precursor for cordierite ceramics [J]. Applied Clay Science, 2004, 27(3): 187–198.
- [51] JIN Jiao, LIU Shuai, GAO Yu-chao, LIU Ruo-hua, HUANG Wang, WANG Li, XIAO Ting, LIN Fei-peng, XU Long-hua, ZHENG Jian-long. Fabrication of cooling asphalt pavement by novel material and its thermodynamics model [J]. Construction and Building Materials, 2021, 272: 121930.
- [52] EREN E, AFSIN B. An investigation of Cu(II) adsorption by raw and acid-activated bentonite: A combined potentiometric, thermodynamic, XRD, IR, DTA study [J]. Journal of Hazardous Materials, 2008, 151(2): 682–691.
- [53] JIN Jiao, GAO Yu-chao, WU Yin-rui, LIU Shuai, LIU Ruo-hua, WEI Hui, QIAN Guo-ping, ZHENG Jian-long. Rheological and adhesion properties of nano-organic palygorskite and linear SBS on the composite modified asphalt [J]. Powder Technology, 2021, 377: 212–221.

## 锂辉石浮选尾矿低温烧结制备多孔陶瓷及其性能

杨洁<sup>1</sup>, 徐龙华<sup>1,2</sup>, 巫侯琴<sup>1,3</sup>, 金娇<sup>4</sup>

1. 西南科技大学 固体废物处理与资源化教育部重点实验室, 绵阳 621010;
2. 西南科技大学 环境友好能源材料国家重点实验室, 绵阳 621010;
3. 西南科技大学 土木工程与建筑学院, 绵阳 621010;
4. 长沙理工大学 交通运输工程学院, 长沙 410114

**摘要:** 以锂辉石浮选尾矿(SFT)、高岭土和低熔点玻璃粉(LPG)为原料, 通过过氧化氢(H<sub>2</sub>O<sub>2</sub>)发泡法制备多孔陶瓷。添加 LPG 以降低多孔陶瓷的烧结温度, 添加高岭土使多孔陶瓷对亚甲基蓝具有吸附性。多孔陶瓷平均抗折强度、抗压强度、显气孔率、吸水率和亚甲基蓝最大吸附量分别为 5.60 MPa、4.66 MPa、52.27%、44.32%和 0.7 mg/g。正交试验结果表明, 烧结温度和 H<sub>2</sub>O<sub>2</sub> 用量分别对多孔陶瓷的力学性能和显气孔率有较大影响。随着烧结温度的升高, LPG 逐渐软化, 把矿物颗粒紧密地粘附在一起, 这是多孔陶瓷力学性能提高的主要原因。高岭石在 550 °C 时没有完全转化为偏高岭石, 这可能是多孔陶瓷具有吸附性的主要原因。

**关键词:** 锂辉石浮选尾矿; 多孔陶瓷; 低温烧结; 吸附

(Edited by Bing YANG)